High-order phonon scattering and phonon coherence in 2D puckered penta-PdPSe sheet

Asghar Hussain, Chenxin Zhang, and Qian Wang*
School of Materials Science and Engineering, Peking University, Beijing 100871, China

(Received 16 May 2025; accepted 25 November 2025; published 24 December 2025)

Motivated by the experimental synthesis of the first ternary penta-PdPSe sheet [P. Li, *et al.*, Adv. Mater. **33**, 2102541 (2021)], we investigate its high-order phonon scattering and phonon coherence, along with their impact on the lattice thermal conductivity using first-principles calculations combined with the unified theory of thermal transport. The penta-PdPSe sheet is semiconducting with an indirect band gap of 1.94 eV at the HSE06 level. Our calculated results reveal that four-phonon scattering plays an important role in suppressing the lattice thermal conductivity. When four-phonon scattering is considered, the particle-like thermal conductivity κ_L^P at 300 K is reduced by 54.70% along the *x*-direction and 59.05% along the *y*-direction. This reduction is primarily due to the strong scattering of acoustic phonons, which contributes approximately 88.50% to the particle-like lattice thermal transport. The phonon lifetime of acoustic modes of phonon is greater than the Wigner limit in time, resulting in a small contribution from phonon coherent transport. The total lattice thermal conductivity, incorporating both phonon scattering and coherence effects, exhibits anisotropic values of 6.20 $\mathrm{W\,m^{-1}\,K^{-1}}$ along the *x*-direction and 7.68 $\mathrm{W\,m^{-1}\,K^{-1}}$ along the *y*-direction at 300 K. The low lattice thermal conductivity arises from the large mass contrast between Pd and P/Se atoms, weak interatomic bonding, and puckered pentagonal geometry, which collectively enhance anharmonicity and phonon scattering. Our work provides new insights into the low lattice thermal transport properties of the first synthesized ternary penta-sheet.

DOI: 10.1103/jdd4-v9xb

I. INTRODUCTION

Pentagons, as distinctive geometric structural units, have revolutionized the design of advanced materials. Since the prediction of penta-graphene in 2015 [1], the field of pentagonal materials has grown rapidly, with nearly 200 pentagon-based structures proposed over the past decade [2,3], which have evolved from elemental atoms as structural building blocks to complex molecules and clusters. These materials exhibit unique mechanical, electronic, and optical properties that fundamentally differ from those of conventional hexagon-based systems. These distinctive characteristics are also reflected in their thermal transport behavior. Specifically, the lack of high rotational and mirror symmetries in pentagonal lattices relaxes the selection rules governing three- and four-phonon scattering processes, thus enlarging the momentum- and energy-conserving phase space. The enhancement of Umklapp scattering rates typically leads to a pronounced suppression of lattice thermal conductivity. For instance, the lattice thermal conductivity of penta-NiN_2 was reported to be 11.67 $\mathrm{W\,m^{-1}\,K^{-1}}$ at room temperature, but after considering four-phonon (4-ph) scattering, its value is reduced by 89.32% compared to considering only three-phonon (3-ph) processes [4], demonstrating the critical role of 4-ph interactions. Conversely, phonon coherence has been identified as the main controlling mechanism for the lattice thermal conductivity of pentagonal PbN_8 sheets [5]. Furthermore, penta-sheets feature anisotropic bonding and structural puckering, which split acoustic branches, mix acoustic and optical characteristics, and induce mode anisotropy and avoided crossings, thus resulting in strongly direction-dependent lattice thermal conductivity.

Theoretical progress has strongly stimulated the experimental synthesis of pentagonal materials. Beyond previously synthesized binary penta-sheets such as penta-$PdSe_2$ [6], penta-NiN_2 [7], and penta-$PdTe_2$ [8], the first ternary pentagonal sheet, penta-PdPSe, was successfully realized via mechanical exfoliation [9]. Compared with its binary counterpart penta-$PdSe_2$, the ternary penta-PdPSe exhibits several unique features. Structurally, PdPSe comprises three atomic species (Pd, P, and Se) arranged in a puckered, non-centrosymmetric framework, where each Pd atom is coordinated to two Se and two P atoms forming a $[\mathrm{Se-P-P-Se}]^{4-}$ polyanionic motif. This configuration breaks both mirror and inversion symmetries, thereby relaxing phonon selection rules and introducing substantial bond length and bond angle variations that enhance anharmonicity and phonon coupling. In addition, the ternary composition introduces pronounced atomic mass and bonding contrast (Pd > Se > P), which would broaden the phonon spectrum, promote overlapping acoustic and optical modes, and intensify 4-ph Umklapp scattering. Moreover, the mixed-anion environment can produce quasi-degenerate and hybridized phonon branches, fostering coherent phonon transport. In this regime, heat may propagate partly through phase-preserving wave-like phonons rather than completely random phonon scattering, giving rise to an enhanced coherence-driven contribution to lattice thermal conductivity.

Altogether, penta-PdPSe offers a low-symmetry, multi-atomic-mass, and strongly anharmonic lattice environment that provides an ideal platform for uncovering the interplay

*Contact author: qianwang2@pku.edu.cn

between high-order phonon scattering and phonon coherence in complex pentagonal systems—an area that has remained largely unexplored to date. In this work, we conduct a comprehensive theoretical investigation to elucidate how high-order phonon scattering and phonon coherence affect the lattice thermal conductivity of penta-PdPSe, thereby addressing aspects of its thermal-transport behavior that have not been examined in previous studies [10].

II. METHODS

First-principles calculations are performed within the framework of density functional theory (DFT) by using the projector-augmented wave method (PAW) implemented in the Vienna *ab initio* simulation package (VASP) [11]. The exchange-correlation functional is treated by using the Perdew-Burke-Ernzerhof functional (PBE) [12], while the Heyd-Scuseria-Ernzerhof (HSE06) [13] functional is used for more accurate bandgap calculations. A kinetic energy cut-off of 600 eV is applied for the plane-wave basis set. The Brillouin zone is sampled using a $9 \times 9 \times 1$ Gamma-centered **k**-point mesh for geometry optimization. Convergence criteria for energy and forces are set to 10^{-8} eV and 10^{-6} eV/Å, respectively. To avoid interactions between periodic images of the penta-PdPSe sheet, a vacuum space of 20 Å is introduced perpendicular to the sheet.

The total lattice thermal conductivity κ_L is calculated by using the unified theory of thermal transport [14–16], which considers the contributions from both phonon scattering (κ_L^P) and phonon coherence (κ_L^C):

$$\kappa_L = \kappa_L^P + \kappa_L^C \tag{1}$$

The κ_L^P is obtained by solving the Boltzmann transport equation (BTE) [17], under the framework of 3- and 4-phonon scattering:

$$\kappa_L^{P,\alpha\beta} = \frac{1}{k_B T^2 \Omega N} \sum_{\mathbf{q}} \sum_i \bar{N}(\mathbf{q})_i (\bar{N}(\mathbf{q})_i + 1)(\hbar\omega(\mathbf{q})_i)^2 \times V^\alpha(\mathbf{q})_i V^\beta(\mathbf{q})_i \tau(\mathbf{q})_i \tag{2}$$

where α and β denote the Cartesian coordinates; k_B, T, Ω, N, and $\hbar$ represent the Boltzmann constant, absolute temperature, unit cell volume, number of discrete **q**-points in the Brillouin zone, and the reduced Planck constant, respectively. The terms $\omega(\mathbf{q})_i$, $\tau(\mathbf{q})_i$, and $\bar{N}(\mathbf{q})_i$ correspond to the angular frequencies, phonon lifetime, and equilibrium Bose-Einstein distribution of the phonon mode indexed by wave vector **q** and branch i, respectively. The calculations of κ_L^P are performed using the SHENGBTE package [18], with harmonic (second-order) and anharmonic (third- and fourth-order) interatomic force constants (IFCs) as inputs. The phonon dispersion is obtained by using the PHONOPY package [19], with the finite displacement method, employing a $3 \times 3 \times 1$ supercell and a $3 \times 3 \times 1$ **k**-point mesh. Perturbative structures of the penta-PdPSe sheet for calculating third- and fourth-order IFCs are generated by using the Monte-Carlo random displacement method implemented in the HIPHIVE package [20]. The cut-off distances for the second-, third-, and fourth-order IFCs are set to 8.00 Å, 5.00 Å, and 4.00 Å, respectively. The thickness of the penta-PdPSe sheet is set to 7.60 Å, accounting for the buckling of the sheet and van der Waals radius [21,22]. In solving the Boltzmann transport equation for phonons, the **q**-mesh of $40 \times 40 \times 1$ and $9 \times 9 \times 1$ is used for the third- and higher-order calculations, respectively (see Fig. S1 of the Supplemental Material for **q**-mesh used for convergent SHENGBTE calculations [23]). The phonon coherence contribution (κ_L^C) is calculated by using the phonon coherence equation [24].

$$\kappa_L^{C,\alpha\beta} = \frac{\hbar^2}{k_B T^2 \Omega N} \sum_{\mathbf{q}} \sum_{i \neq j} \frac{\omega(\mathbf{q})_i + \omega(\mathbf{q})_j}{2} V^\alpha(\mathbf{q})_{ij} V^\beta(\mathbf{q})_{ji} \times \frac{\omega(\mathbf{q})_i \bar{N}(\mathbf{q})_i (\bar{N}(\mathbf{q})_i + 1) + \omega(\mathbf{q})_j \bar{N}(\mathbf{q})_j (\bar{N}(\mathbf{q})_j + 1)}{4(\omega(\mathbf{q})_i - \omega(\mathbf{q})_j)^2 + (\Gamma(\mathbf{q})_i + \Gamma(\mathbf{q})_j)^2} \times (\Gamma(\mathbf{q})_i + \Gamma(\mathbf{q})_j) \tag{3}$$

where $\Gamma(\mathbf{q})_i = 1/\tau(\mathbf{q})_i$ represents the phonon linewidth (scattering rate) of each phonon mode. The total phonon scattering rates ($\Gamma(\mathbf{q})_i$) include contributions from 3-ph (τ_3^{-1}) and 4-ph scattering rates (τ_4^{-1}):$\Gamma(\mathbf{q})_i = \tau_3^{-1} + \tau_4^{-1}$. The off-diagonal velocity matrix ($V(\mathbf{q})_{ij}$), the generalized lifetime matrix ($\tau(\mathbf{q})_{ij}$), and the Bose-Einstein distribution $\bar{N}(\mathbf{q})_i$ are calculated as follows:

$$V(\mathbf{q})_{ij} = \frac{1}{\omega(\mathbf{q})_i + \omega(\mathbf{q})_j} \langle e(\mathbf{q})_i | \frac{\partial D(\mathbf{q})}{\partial \mathbf{q}} | e(\mathbf{q})_j \rangle \tag{4}$$

$$\tau(\mathbf{q})_{ij} = \frac{2(\Gamma(\mathbf{q})_i + \Gamma(\mathbf{q})_j)}{4(\omega(\mathbf{q})_i - \omega(\mathbf{q})_j)^2 + (\Gamma(\mathbf{q})_i + \Gamma(\mathbf{q})_j)^2} \tag{5}$$

$$\bar{N}(\mathbf{q})_i = \frac{1}{e^{\frac{\hbar\omega(\mathbf{q})_i}{k_B T}} - 1} \tag{6}$$

In Eq. (4), $e(\mathbf{q})_i$ is the eigenvector of the phonon mode i, and $D(\mathbf{q})$ is the dynamical matrix of the crystal with an eigenvalue of $\omega(\mathbf{q})_i$. The calculations for κ_L^C are performed using an in-house code.

III. RESULTS AND DISCUSSIONS

A. Geometric structure, dynamical stability, and electronic properties

The geometric structure of the penta-PdPSe sheet, depicted in Fig. 1(a), exhibits a buckling height of 4.24 Å. The lattice structure consists of a pentagonal primitive unit cell containing twelve atoms (4-Pd, 4-P, and 4-Se) as highlighted in a red square. The unit cell adopts an orthorhombic symmetry possessing a space group of *Pbcn* (No. 60) with lattice constants $a = 5.86$ Å and $b = 5.91$ Å. Each Pd atom is coordinated in a planar arrangement shown in a red square, surrounded by two Se atoms and two phosphorus atoms, forming a pentagonal pattern in the top view, as shown in Fig. 1(a).

To assess the dynamical stability of the penta-PdPSe sheet, we first calculate its phonon dispersion spectrum. A structure is dynamically stable if its phonon dispersion exhibits exclusively positive frequencies throughout the Brillouin zone, whereas negative frequencies indicate structural instability due to insufficient restoring forces against atomic displacements. As shown in Fig. 1(b), the absence of imaginary phonon modes across the entire first Brillouin zone confirms the dynamical stability of the penta-PdPSe sheet. The phonon spectrum consists of 36 vibrational modes corresponding to

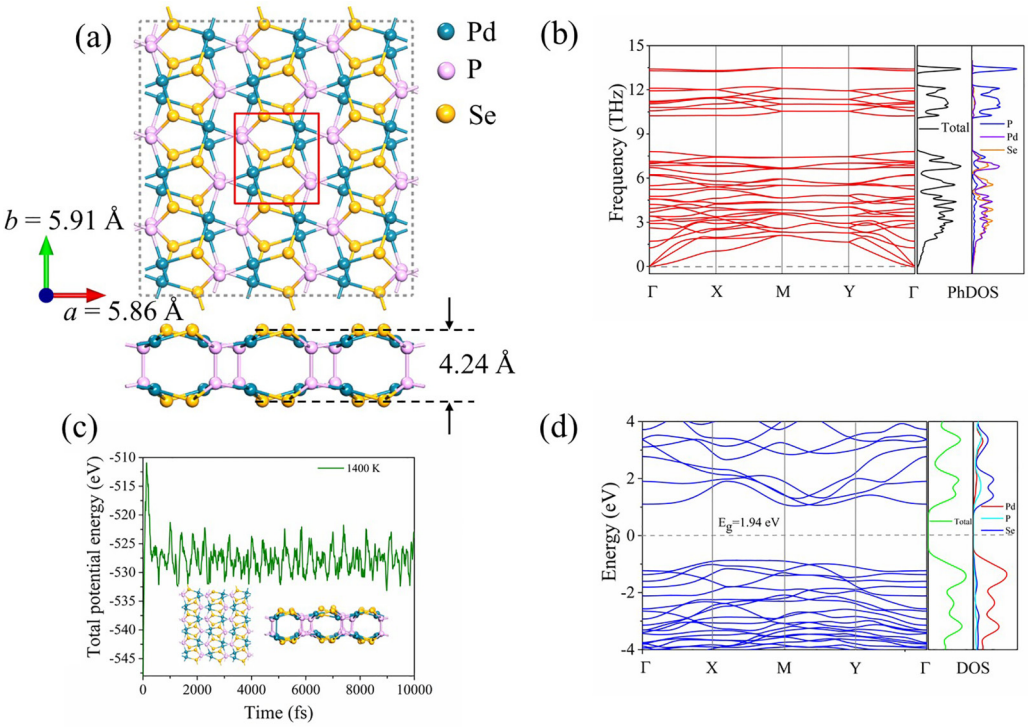

FIG. 1. (a) Top and side view of the optimized geometry of the penta-PdPSe sheet. The red rectangle indicates the planar primitive unit cell. (b) Phonon spectra and PhDOS, (c) Variation of the total potential energy with simulation time in AIMD simulation at 1400 K, and top and side views of the geometry at the end of the simulation, and (d) band structure and total and partial DOS of the penta-PdPSe sheet.

the 12 atoms in the unit cell, including 33 optical modes and 3 acoustic modes in the low-frequency region. Figure 1(b) reveals a phonon spectrum that consists of an overlap of in-plane transverse (TA) and longitudinal (LA) acoustic modes. LA shows the linear dispersion, while ZA depicts the out-of-plane flexural mode that exhibits quadratic dispersion in the long-wavelength limit. The quadratic dispersion of the ZA leads to a high phonon density of states, which enhances its contribution to heat transport compared to the LA and TA modes. The out-of-plane, ZA acoustic mode originates from the Γ point within the high Brillouin zone of the penta-PdPSe sheet. These ZA acoustic modes are typically the primary heat carriers and play a crucial role in the lattice thermal transport properties of the penta-PdPSe sheet. Additionally, a wide gap emerges in the phonon dispersion spectrum from 7.80 THz – 10.23 THz, implying a reduction in group velocity, which further contributes to the low lattice thermal conductivity. To further analyse the phonon dispersion spectrum, we calculate the phonon density of states (PhDOS) shown in Fig. 1(b), in which the Pd and Se atoms primarily contribute to the acoustic and low-frequency optical modes, whereas the high-frequency optical modes mainly originate from the P atoms. The low-frequency phonon modes are attributed to the large mass of Pd and Se atoms having weak interatomic bonds, possessing strong anharmonicity that enhances the phonon-phonon scattering. As a result, the phonon lifetime is reduced, thereby suppressing lattice thermal conductivity. Similar trends have been observed in previous studies, where atomic mass contrast was shown to strengthen anharmonicity and significantly impact thermal transport properties [25–29].

To verify the thermal stability of the penta-PdPSe sheet, we performed *ab initio* molecular dynamics (AIMD) simulations at 1400 K employing a $3 \times 3 \times 1$ supercell for 10 ps with a time step of 1 fs. As shown in Fig. 1(c), the total energy exhibits only minor fluctuations throughout the simulation without visible structural distortions or bond breakage. This indicates that the penta-PdPSe sheet maintains its structural integrity even under high-temperature conditions. The inset in Fig. 1(c) shows the top and side views of the optimized lattice structure after 10 ps, further confirming its thermal robustness at elevated temperatures.

Next, we evaluate the mechanical stability of the penta-PdPSe sheet by computing the stiffness tensor components, C_{ij} (i, j = 1, 2, 6), using the finite distortion method [30]. The calculated independent elastic constants are $C_{11} = 111.11$, $C_{22} = 144.07$, $C_{66} = 42.68$, $C_{12} = 19.21$, $C_{16} = -0.11$, and $C_{26} = -0.11\,\mathrm{N\,m^{-1}}$. These values satisfy the Born-Huang stability criteria for an orthorhombic 2D material [31], confirming the mechanical stability of the penta-PdPSe sheet (see Note S1 in the Supplemental Material for further details on the calculation of the stiffness tensor components [23]).

We investigate its electronic band structure using the HSE06 functional. Figure 1(d) shows that the electronic band structure exhibits semiconducting behavior with an indirect band gap of 1.94 eV, suggesting that phonons dominate the thermal transport in penta-PdPSe. By analyzing the total and partial density of states (DOS), we find that the Pd atoms predominantly contribute to the electronic states in the valence band near the Fermi level, whereas electronic states in the conduction band arise from the contribution of Pd, Se, and P

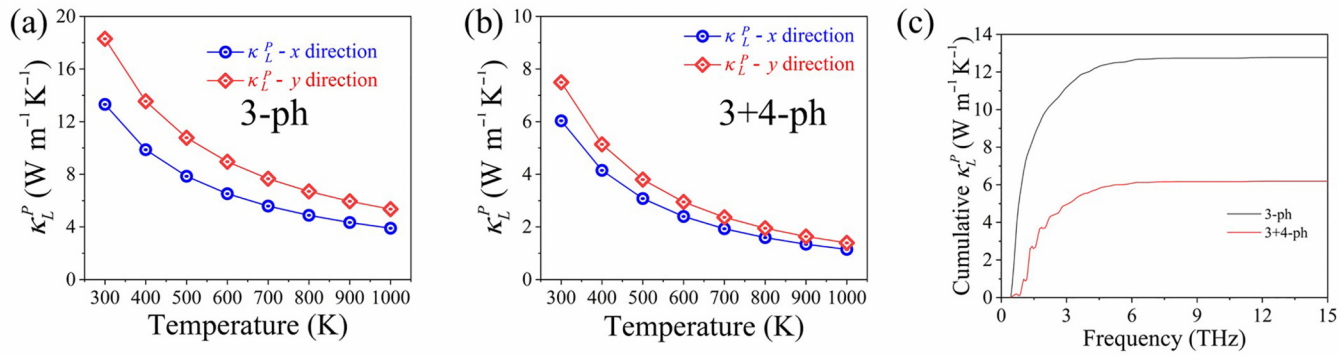

FIG. 2. Lattice thermal conductivity (κ_L^P) considering (a) only 3-ph scattering and (b) 3+4-ph scattering. (c) Cumulative κ_L^P versus phonon frequency at 300 K of the penta-PdPSe sheet.

atoms. Our calculated band gap aligns well with experimental results reported by Li, *et al.* [9].

B. Impact of 4-ph scattering on the lattice thermal conductivity

Given the semiconducting nature of the penta-PdPSe sheet, the thermal conductivity contributed by electrons can be neglected. Therefore, we calculate the lattice thermal conductivity κ_L using the unified theory of thermal transport [32], which accounts for both phonon scattering (κ_L^P) and phonon coherence (κ_L^C). A similar theoretical framework has been successfully employed to analyze the thermal transport properties of the experimentally reported bilayer penta-NiN_2 [33] and $PdSe_2$ [34], further supporting the applicability of this method to pentagonal materials. Although the lattice thermal conductivity of the penta-PdPSe sheet has been studied previously [35], the contributions from high-order phonon scattering and coherence remain unexplored. We have calculated the κ_L^P of the penta-PdPSe sheet in different directions, considering the 3-ph and both the 3-ph and 4-ph scattering. Considering only the 3-ph scattering, as illustrated in Fig. 2(a), the calculated values of κ_L^P are 13.31 W m^{-1} K^{-1} and 18.29 W m^{-1} K^{-1} at 300 K along the x- and y-directions, respectively, showing an obvious anisotropy. The 3-ph values we obtain are smaller than the previously reported 44 and 65 W m^{-1} K^{-1} [35] based on a moment tensor potential (MTP). We attribute this discrepancy to differences in the evaluation of interatomic forces between the MTP model and our DFT-based approach. However, when including the 4-ph scattering into account in calculations, as shown in Fig. 2(b), the corresponding κ_L^P is decreased to 6.03 W m^{-1} K^{-1} and 7.49 W m^{-1} K^{-1}, respectively, corresponding to a 54.70% reduction along the x-direction and a 59.05% reduction along the y-direction. This suggests that the 4-ph interactions result in stronger scattering events, leading to shorter phonon lifetime, thus suppressing thermal transport. In addition, the cumulative κ_L^P as a function of frequency is calculated and plotted in Fig. 2(c), which shows that the phonons with their frequencies lower than 2.50 THz contribute more than 88.50% to the κ_L^P. To understand the exact effects of 4-ph scattering on the lattice anharmonicity and its temperature dependence, we calculate the phonon scattering rates of penta-PdPSe within the 3-ph and 3+4-ph levels, as shown in Figs. 3(a) and 3(b).

Figures 3(a) and 3(b) show the scattering rates of the 3-ph and the 4-ph scattering at 300 K and 900 K, respectively. At 300 K, the inclusion of 4-ph interactions leads to a notable increase in scattering rates, particularly for acoustic and low-frequency optical phonons. In this region, the 4-ph scattering rates are significantly higher than those of 3-ph scattering processes, highlighting the crucial role of higher-order anharmonicity in limiting phonon lifetimes. To further elucidate the contribution of acoustic and optical phonons to κ_L^P, the low-frequency acoustic modes are analysed (see Fig. S2 of the Supplemental Material [23]). At 300 K, the 4-ph interactions enhance the scattering rates by nearly an order of magnitude in the low-frequency regime, reflecting stronger phonon-phonon interactions, which effectively hinder phonon propagation and thereby reduce the lattice thermal conductivity. As the temperature increases to 900 K, a broader range of phonon modes becomes thermally activated, leading to intensified anharmonic interactions for further suppressing the thermal conductivity at elevated temperatures. Furthermore, Fig. 3(c) illustrates that the penta-PdPSe sheet exhibits a low phonon group velocity with a maximum value of 5.86 km s^{-1}, which

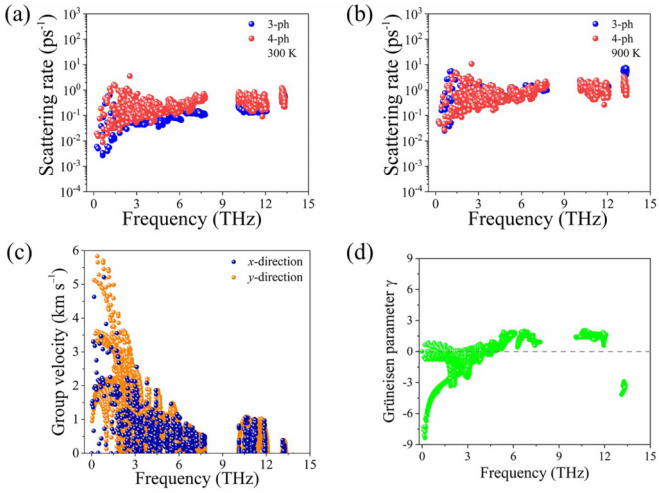

FIG. 3. Calculated intrinsic 3-ph (blue points) and 4-ph (red dots) scattering rates at (a) 300K and (b) 900 K, (c) phonon group velocity along different axes, and (d) Grüneisen parameters of the penta-PdPSe sheet.

is significantly lower than other 2D pentagonal materials such as penta-graphene (17.17 km s^{-1}) [36], and penta-C_3N (22.20 km s^{-1}) [37]. These results suggest that the relatively large atomic size of Pd weakens the Pd-P and Pd-Se bonds compared to the C-C, and C-N bonds in other materials. From the calculated stiffness tensor and 2D Young's moduli (See Note S1 of the Supplemental Material [23]), we infer that the reduction of group velocity originates from the large atomic masses of Pd and Se atoms and the relatively weak interatomic bonding, consistent with the observations in penta-PtPX (X = S, Se, Te) nanosheets [38]. The weak bonding interactions suppress the phonon dispersion, reduce group velocities, and enhance phonon scattering rates. The variation in the phonon group velocity illustrates the origin of the directional dependence of the lattice thermal conductivity, which is influenced by the anisotropic nature of its geometric structure. Due to the high scattering rates and the low group velocity, the κ_L^P exhibits a relatively low value. The significant mass difference between Pd and P/Se atoms, combined with the high mass of Pd, enhances phonon scattering, contributing to stronger lattice anharmonicity and the suppressed group velocity, further intensifying phonon-phonon interactions, which is also demonstrated by the large Grüneisen parameter (γ) shown in Fig. 3(d). A similar effect appears in previous studies on materials such as perovskite $CH_3NH_3PbI_3$, where the pronounced mass contrast led to strong coupling between phonons in different frequency regions, resulting in enhanced phonon anharmonicity [39].

C. Impact of phonon coherence on the lattice thermal conductivity

In materials with low κ_L, the wavelike phonon tunneling effect is a significant phenomenon that attracts much attention [40]. Thus, to gain a better understanding of the lattice thermal transport properties in the penta-PdPSe sheet, it is necessary to thoroughly investigate the phonon coherence contributions (κ_L^C) to κ_L. The calculated lattice thermal conductivity considering only the 3-ph scattering is presented (see Figs. S3(a) and S3(b) of the Supplemental Material [23]). At 300 K, the κ_L^C values are 0.16 W m^{-1} K^{-1} along the x-direction and 0.30 W m^{-1} K^{-1} along the y-direction, respectively, and the corresponding κ_L values are 13.47 W m^{-1} K^{-1} along the x-direction and 18.59 W m^{-1} K^{-1} along the y-direction. These results demonstrate that when only 3-ph scattering is considered, the contribution of κ_L^C is small. Additionally, to obtain more accurate results, we calculated the κ_L^C and κ_L considering both 3-ph and 4-ph interactions. As shown in Figs. 4(a) and 4(b), one can see that κ_L^C values are 0.17 W m^{-1} K^{-1} and 0.19 W m^{-1} K^{-1}, along the x- and y-directions, respectively. According to Eq. (1), at 300 K, the κ_L reaches 6.20 W m^{-1} K^{-1} along the x-direction and 7.68 W m^{-1} K^{-1} along the y-direction. As a consequence, the κ_L^C values are only about 2.74% and 2.47% in the x- and y-directions, respectively, showing relatively low contributions. Moreover, as shown in Fig. 4(b), the lattice thermal conductivity of the penta-PdPSe sheet decreases monotonically with increasing temperature. This behavior is consistent with that of phonon-dominated crystalline materials [41].

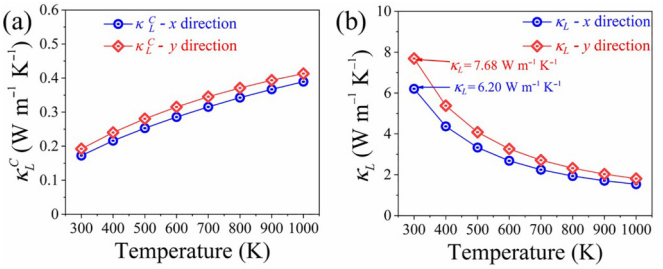

FIG. 4. Lattice thermal conductivity (κ_L^C) with (a) both 3- and 3+4-ph scattering and (b) total lattice thermal conductivity (κ_L) of the penta-PdPSe sheet at different temperatures.

To identify which phonon modes contribute most significantly to coherence transport, we analyzed the two-mode-dependent contributions in κ_L^C from the coupling phonon frequencies ω_1 and ω_2 in the penta-PdPSe sheet. The involvement of degenerate ($\omega_1 = \omega_2$) and nondegenerate ($\omega_1 \neq \omega_2$) eigenstates across various temperature ranges is illustrated in Figs. 5(a)–5(d), where the red dashed lines indicate the degenerate modes ($\omega_1 = \omega_2$) along the diagonal, primarily contributing to κ_L^C. In contrast, the contributions from the nondegenerate modes ($\omega_1 \neq \omega_2$) are not dominant. Degenerate eigenstates exhibit sufficient scattering rates, enabling them to contribute significantly to κ_L^C. The dominance of degenerate eigenstates suggests that phonons with identical frequencies couple with each other strongly and sustain wave-like tunnelling, largely dictated by their lifetime and scattering rates. It is worth noting that phonons with frequencies below 2.50 THz play a significant role in the coherent thermal transport at 300 K, indicating the strong coupling between low-frequency acoustic and low-energy optical phonons. These low-energy modes typically exhibit longer lifetime and lower scattering rates, enabling to maintain phase relationships necessary for coherent transport. As the temperature increases to 500, 800, and 1000 K, there is a monotonic increase in the coherent contribution from the nondegenerate eigenstates, as clearly observed in Figs. 5(b)–5(d). This phenomenon arises from the temperature-dependent enhancement of the phonon scattering ($\Gamma(\mathbf{q})_i$), as described in Eq. (5). The lifetime of the coherent phonon modes is inversely proportional to their scattering rates and depends on the frequency difference intervals. Importantly, as temperature increases, the phonon-phonon scattering increases, leading to a significant reduction in phonon lifetime. This trend is evident (see Fig. S4 of the Supplemental Material for scattering rates considering both 3- and 4-ph interactions at temperatures 300, 500, 800, and 1000 K [23]), which illustrates the temperature dependence of scattering rates and highlights the decline in phonon lifetime, thereby suppressing the contributions of degenerate eigenstates. To gain deeper insight, we then discussed the relationship between the lifetime of phonon modes (τ_i) and their contribution to κ_L^C.

To better understand the above results, we analyze the relationship between phonon lifetime and the criteria distinguishing scattering and coherence contributions at 300 K, as shown in Fig. 6. The expression $1/\Delta\omega_{\text{ave}} = 3N_{\text{at}}/\omega_{\max}$ is used to define the Wigner limit in time [42], which serves as a temporal boundary between phonon coherence and scattering.

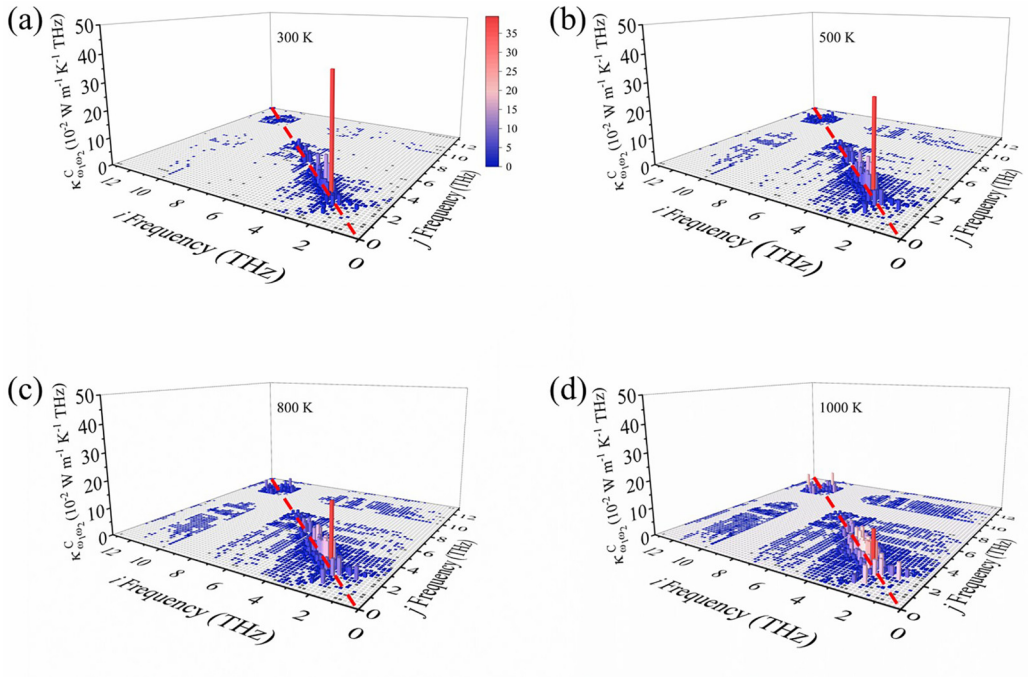

FIG. 5. (a)–(d) Two-mode-dependent contributions to κ_L^C versus the coupling phonon frequencies ω_1 and ω_2 at temperature from 300 to 1000 K, respectively, in the penta-PdPSe sheet.

In this expression, $\Delta\omega_{\text{ave}}$, N_{at}, and ω_{max} represent the average frequency interval, the number of atoms in the unit cell, and the maximum phonon frequency, respectively. Phonon modes with τ shorter than this threshold contribute to the coherent part of the lattice thermal conductivity [43], while the Ioffe-Regel limit ($1/\omega$) provides a reference for evaluating the breakdown of the phonon quasiparticle approximation [42]. Although many phonon lifetimes lie above the Wigner limit, this does not contradict the presence of strong anharmonicity indicated by the influence of 4-ph scattering. The Wigner limit distinguishes between the dominance of coherent and scattering transport mechanisms, but it does not necessarily reflect the degree of anharmonicity. Our results clearly show that the inclusion of 4-ph scattering significantly reduces phonon lifetimes, particularly in the low- and mid-frequency ranges, confirming strong anharmonic interactions that make the major contribution to the κ_L^P. The heavy masses, large atomic size, and significant differences in atomic mass and size in penta-PdPSe result in weak bonding and enhanced phonon-phonon scattering. This, in turn, reduces the phonon lifetime and further suppresses κ_L^P. The low-frequency degenerate modes, which have lifetimes exceeding the Wigner limit, contribute to coherent phonon transport. These mechanisms collectively lead to the low lattice thermal conductivity of penta-PdPSe, with phonon scattering as the dominant factor.

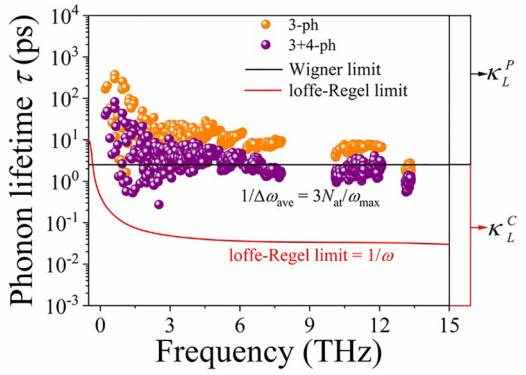

FIG. 6. Comparison of phonon lifetime between the 3-ph and the 3+4-ph scattering at 300 K. The black solid line depicts the Wigner limit in time. The red curve is the Ioffe-Regel limit, which is calculated by $1/\omega$.

IV. CONCLUSIONS

In summary, we investigate the influence of 3- and 4-ph interactions and the contributions of phonon scattering and coherence on the lattice thermal transport properties of the penta-PdPSe sheet, which exhibits intrinsically low and anisotropic lattice thermal conductivity with values of 6.20 $\text{W m}^{-1}\text{K}^{-1}$ (x-direction) and 7.68 $\text{W m}^{-1}\text{K}^{-1}$ (y-direction) at 300 K, arising from strong anharmonicity caused by the large mass contrast between Pd and P/Se atoms, weak interatomic bonding, and narrow phonon band dispersions. The 4-ph scattering plays a dominant role, reducing the lattice thermal conductivity by 54.70% (x-direction) and 59.05% (y-direction) compared to the 3-ph scattering processes, underscoring the necessity of including high-order scattering. Moreover, the phonon coherence contributions are small as most of the phonon modes lie above the Wigner limit in time, with degenerate eigenstates ($\omega_1 = \omega_2$) dominating at low frequencies (<2.50 THz). These results can be explained by the effect of pentagonal geometry, which reduces symmetry, distorts the bond angles and structural buckling,

thus significantly influencing vibrational behavior. Since the pentagonal geometry introduces internal strain, leading to weaker bond strength and softer phonon modes and lower vibrational frequencies when compared to hexagonal systems. Moreover, the lower symmetry of the pentagonal lattice removes degeneracies in the phonon spectrum, resulting in more vibrational branches with rich and complex phonon structure, while the buckling in the lattice modifies the out-of-plane (ZA) modes and enhances anharmonic effects, resulting in enhanced phonon-phonon scattering and short lifetimes. These factors contribute to lower phonon group velocities and reduce thermal conductivity, distinguishing pentagonal materials from their more symmetric hexagonal counterparts. This work provides a significant understanding of the low lattice thermal transport of the first synthesized ternary penta-structured semiconductor.

ACKNOWLEDGMENTS

This work was partially supported by grants from the National Natural Science Foundation of China (Grant No. NSFC-12274007) and was also supported by the High-Performance Computing Platform of Peking University, China.

DATA AVAILABILITY

The data that support the findings of this article are not publicly available upon publication because it is not technically feasible, and/or the cost of preparing, depositing, and hosting the data would be prohibitive within the terms of this research project. The data are available from the authors upon reasonable request.

[1] S. Zhang, J. Zhou, Q. Wang, X. Chen, Y. Kawazoe, and P. Jena, Penta-graphene: A new carbon allotrope, Proc. Natl Acad. Sci. USA **112**, 2372 (2015).

[2] Y. Shen and Q. Wang, Pentagon-based 2D materials: Classification, properties and applications, Phys. Rep. **964**, 1 (2022).

[3] M. A. Nazir, A. Hassan, Y. Shen, and Q. Wang, Research progress on penta-graphene and its related materials: Properties and applications, Nano Today **44**, 101501 (2022).

[4] C. Zhang, J. Sun, Y. Shen, W. Kang, and Q. Wang, Effect of high-order phonon scattering on the thermal conductivity and its response to strain of a penta-NiN_2 sheet, J. Phys. Chem. Lett. **13**, 5734 (2022).

[5] A. Hussain, C. Zhang, P.-H. Du, Q. Sun, and Q. Wang, Theoretical studies on the strong phonon coherence in the type-5 penta-PbN_8 sheet, J. Mater. Chem. C **13**, 7836 (2025).

[6] W. L. Chow, P. Yu, F. Liu, J. Hong, X. Wang, Q. Zeng, C. H. Hsu, C. Zhu, J. Zhou, and X. Wang, High mobility 2D palladium diselenide field-effect transistors with tunable ambipolar characteristics, Adv. Mater. **29**, 1602969 (2017).

[7] M. Bykov, E. Bykova, A. V. Ponomareva, F. Tasnadi, S. Chariton, V. B. Prakapenka, K. Glazyrin, J. S. Smith, M. F. Mahmood, and I. A. Abrikosov, Realization of an ideal Cairo tessellation in nickel diazenide NiN_2: High-pressure route to pentagonal 2D materials, ACS Nano **15**, 13539 (2021).

[8] L. Liu, Y. Ji, M. Bianchi, S. M. Hus, Z. Li, R. Balog, J. A. Miwa, P. Hofmann, A.-P. Li, and D. Y. Zemlyanov, A metastable pentagonal 2D material synthesized by symmetry-driven epitaxy, Nat. Mater. **23**, 1339 (2024).

[9] P. Li, J. Zhang, C. Zhu, W. Shen, C. Hu, W. Fu, L. Yan, L. Zhou, L. Zheng, and H. Lei, Penta-PdPSe: A new 2D pentagonal material with highly in-plane optical, electronic, and optoelectronic anisotropy, Adv. Mater. **33**, 2102541 (2021).

[10] S. Shahabfar, Y. Xia, M. Morshedsolouk, M. Mohammadi, and S. S. Naghavi, Synergistic effect of alloying on thermoelectric properties of two-dimensional PdPQ (Q = S, Se), Phys. Chem. Chem. Phys. **25**, 9617 (2023).

[11] G. Kresse and J. Furthmüller, Efficient iterative schemes for *ab initio* total-energy calculations using a plane-wave basis set, Phys. Rev. B **54**, 11169 (1996).

[12] J. P. Perdew, K. Burke, and M. Ernzerhof, Generalized gradient approximation made simple, Phys. Rev. Lett. **77**, 3865 (1996).

[13] J. Heyd, G. E. Scuseria, and M. Ernzerhof, Hybrid functionals based on a screened Coulomb potential, J. Chem. Phys. **118**, 8207 (2003).

[14] L. Isaeva, G. Barbalinardo, D. Donadio, and S. Baroni, Modeling heat transport in crystals and glasses from a unified lattice-dynamical approach, Nat. Commun. **10**, 3853 (2019).

[15] A. Jain, Multichannel thermal transport in crystalline Tl_3VSe_4, Phys. Rev. B **102**, 201201 (2020).

[16] M. Simoncelli, N. Marzari, and F. Mauri, Wigner formulation of thermal transport in solids, Phys. Rev. X **12**, 041011 (2022).

[17] M. Omini and A. Sparavigna, An iterative approach to the phonon Boltzmann equation in the theory of thermal conductivity, Phys. B: Conden. Matter **212**, 101 (1995).

[18] Z. Han, X. Yang, W. Li, T. Feng, and X. Ruan, FourPhonon: An extension module to ShengBTE for computing four-phonon scattering rates and thermal conductivity, Comp. Phys. Commun. **270**, 108179 (2022).

[19] A. Togo and I. Tanaka, First principles phonon calculations in materials science, Scr. Mater. **108**, 1 (2015).

[20] F. Eriksson, E. Fransson, and P. Erhart, The HIPHIVE package for the extraction of high-order force constants by machine learning, Advan. Theory Simul. **2**, 1800184 (2019).

[21] X. Wu, V. Varshney, J. Lee, Y. Pang, A. K. Roy, and T. Luo, How to characterize thermal transport capability of 2D materials fairly?–Sheet thermal conductance and the choice of thickness, Chem. Phys. Lett. **669**, 233 (2017).

[22] Z. Sun, K. Yuan, X. Zhang, G. Qin, X. Gong, and D. Tang, Disparate strain response of the thermal transport properties of bilayer penta-graphene as compared to that of monolayer penta-graphene, Phys. Chem. Chem. Phys. **21**, 15647 (2019).

[23] See Supplemental Material at http://link.aps.org/supplemental/10.1103/jdd4-v9xb for further details on the calculation of the stiffness tensor components, the q-mesh used for convergent ShengBTE calculations, the acoustic modes, the calculated lattice thermal conductivity considering only the 3-ph scattering, and scattering rates considering both 3- and 4-ph interactions at temperatures 300, 500, 800, and 1000 K.

[24] R. Hanus, J. George, M. Wood, A. Bonkowski, Y. Cheng, D. L. Abernathy, M. E. Manley, G. Hautier, G. J. Snyder, and R. P. Hermann, Uncovering design principles for amorphous-like heat conduction using two-channel lattice dynamics, Mater. Today Phys. **18**, 100344 (2021).

[25] Y.-N. Sun, L. Wang, and C. Wang, Anharmonicity and lattice thermal conductivity of negative thermal expansion materials $Zn(CN)_2$ and $Cd(CN)_2$ by first-principles calculations, Dalton Trans. **54**, 764 (2025).

[26] M. Feng, X. Wang, G. Zhu, C. He, J. Sun, X. Ding, J. Shiomi, Y. Xia, B. Li, and Z. Gao, The relation between the atomic mass ratio and quartic anharmonicity in alkali metal hydrides, Mater. Today Phys. **44**, 101423 (2024).

[27] X. Song, Y. Zhao, J. Ni, S. Meng, and Z. Dai, Thermal transport properties of anisotropic materials RbCaX (X = As, Sb) with strong anharmonicity, Comp. Mater. Sci. **213**, 111618 (2022).

[28] Y. Zhang, S. Gan, J. Li, Y. Tian, X. Chen, G. Su, Y. Hu, and N. Wang, Effect of atomic substitution and structure on thermal conductivity in monolayers H-MN and T-MN (M = B, Al, Ga), Phys. Chem. Chem. Phys. **26**, 6256 (2024).

[29] Y. Wang, Y. Zhao, J. Ni, and Z. Dai, First-principles study of the effects of high-order anharmonicity on the thermal transport properties and thermoelectric effects in the lattice dynamics of 12 new Full–Heusler compounds X_2YTe (X = Na, K, Rb, Cs; Y = Zn, Cd, Hg), Adv. Func. Mater. **34**, 2410983 (2024).

[30] Y. Le Page and P. Saxe, Symmetry-general least-squares extraction of elastic data for strained materials from *ab initio* calculations of stress, Phys. Rev. B **65**, 104104 (2002).

[31] Z.-j. Wu, E.-j. Zhao, H.-p. Xiang, X.-f. Hao, X.-j. Liu, and J. Meng, Crystal structures and elastic properties of superhard IrN_2 and IrN_3 from first principles, Phys. Rev. B-Conden. Matter Mater. Phys. **76**, 054115 (2007).

[32] M. Simoncelli, N. Marzari, and F. Mauri, Unified theory of thermal transport in crystals and glasses, Nat. Phys. **15**, 809 (2019).

[33] C. Zhang, J. Sun, Y. Shen, C. Zhang, Q. Wang, A. Yoshikawa, Y. Kawazoe, and P. Jena, Extremely large response of phonon coherence in twisted penta-NiN_2 bilayer, Small **19**, 2303295 (2023).

[34] C. Zhang, Y. Chen, Q. Wang, and P. Jena, Phonon localization and a Boson-peak-like anomaly in twisted penta-$PdSe_2$ bilayer, Nano Lett. **25**, 8689 (2025).

[35] B. Mortazavi, M. Shahrokhi, X. Zhuang, T. Rabczuk, and A. V. Shapeev, Mechanical, thermal transport, electronic and photocatalytic properties of penta-PdPS, PdPSe and PdPTe monolayers explored by first-principles calculations, J. Mater. Chem. C **10**, 329 (2022).

[36] F. Q. Wang, J. Yu, Q. Wang, Y. Kawazoe, and P. Jena, Lattice thermal conductivity of penta-graphene, Carbon **105**, 424 (2016).

[37] Y. Gao, H. Wang, M. Sun, Y. Ding, L. Zhang, and Q. Li, First-principles study of intrinsic phononic thermal transport in monolayer C_3N, Phys. E: Low-Dimens. Syst. Nanostruc. **99**, 194 (2018).

[38] H. Huang, W. Li, C. Hu, and X. Fan, Promising novel thermoelectric materials: Two-dimensional penta-like PtPX (X = S, Se, Te) nanosheets, J. Mater. Chem. C **11**, 9449 (2023).

[39] L. D. Whalley, J. M. Skelton, J. M. Frost, and A. Walsh, Phonon anharmonicity, lifetimes, and thermal transport in $CH_3NH_3PbI_3$ from many-body perturbation theory, Phys. Rev. B **94**, 220301 (2016).

[40] Q. D. Gibson, T. Zhao, L. M. Daniels, H. C. Walker, R. Daou, S. Hébert, M. Zanella, M. S. Dyer, J. B. Claridge, and B. Slater, Low thermal conductivity in a modular inorganic material with bonding anisotropy and mismatch, Science **373**, 1017 (2021).

[41] T. Liang, P. Zhang, P. Yuan, S. Zhai, and D. Yang, A molecular dynamics study on the thermal conductivities of single-and multi-layer two-dimensional borophene, Nano Fut. **3**, 015001 (2019).

[42] Z. Tong, Y. Zhang, A. Pecchia, C. Yam, L. Zhou, T. Dumitrică, and T. Frauenheim, Predicting the lattice thermal conductivity in nitride perovskite $LaWN_3$ from *ab initio* lattice dynamics, Advan. Sci. **10**, 2205934 (2023).

[43] C. Zhang, J. Sun, J. Cheng, and Q. Wang, Ultralow lattice thermal conductivity in quasi-one-dimensional BiI_3 with suppressed phonon coherence, Phys. Rev. B **110**, 174309 (2024).